

# Investigation of vortex statistics in laminar cavity flow by PIV measurements

by

E. Özsoy<sup>1</sup>, P. Rambaud<sup>2</sup>, A. Stitou<sup>3</sup> & M. L. Riethmuller<sup>2,\*</sup>

2: von Karman Institute for Fluid Dynamics, Chaussée de Waterloo 72, B-1640 Rhode Saint Genèse (Belgium)

1 (Present affiliation): Istanbul Technical University, Institute of Science and Technology,  
Department of Aerospace Engineering 34469 Maslak, Istanbul, (Turkey)

3: ONERA / DMAE Complexe Aérospatial de Lespinet 2, av Edouard Belin BP 4025 31055 Toulouse Cedex  
(France)

\* corresponding author: [riethmuller@vki.ac.be](mailto:riethmuller@vki.ac.be)

## ABSTRACT:

In the present paper, a laminar cavity is analyzed at very low Mach numbers. Characteristics of core-vortices are proposed and commented. The experiments were performed in an open subsonic wind tunnel using particle image velocimetry. A rectangular cavity with a length to depth ratio of four was used (shallow and open type). Three different Reynolds numbers, based on cavity depth and free stream velocity, were examined ( $Re_h=4000, 9000$  &  $13000$ ). The upstream boundary layer was investigated using classical hot-wire anemometry and was found to be laminar. For each Reynolds number a total of one thousand vectors fields were acquired. Results are given in terms of conventional quantities (mean flow velocity, turbulence characteristics, Reynolds shear stress) and also in terms of vortex characteristics (such as probability density function of vortex location, vortex size and vortex circulation). Some of these vortex characteristics are then proposed in a local averaged presentation. The extraction of vortices from instantaneous flow fields has been done through the use of a homemade algorithm based on continuous wavelet analysis.

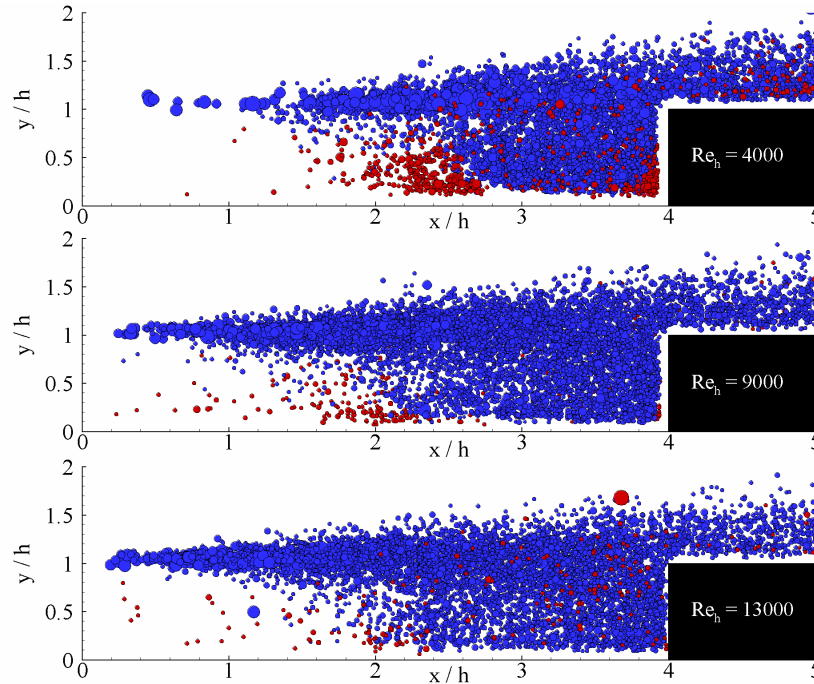


Figure 1: Map of vortex location for an increasing Reynolds number (blue colors= clockwise vortices, red colors= anti-clockwise vortices, arbitrary scale)

## 1. INTRODUCTION

Cavities have been extensively studied in the past because of their unavoidable presence in both industrial and military applications. Dead zones in pipeline gas transport systems and weapons bays are taken here as classical examples. Despite a simple geometrical design, literature about cavities contains various concepts from different fields such as linear and non-linear theory, turbulence, direct or large eddy simulation, aero-acoustic or fluid-structure coupling.

The velocity driven cavity or lid driven cavity has been chosen, years ago, to be a numerical benchmark (Shankar and Deshpande (2000)) when its experimental counter part is the shear driven cavity. Previous reviews collecting extensive works done in this last field had already been proposed by Rockwell and Naudascher (1978) or Komerath et al. (1987). Most of the flows of interest in these compilations were associated with a subsonic, transonic or supersonic Mach number. A relative low number of studies are associated with a very low Mach number (Tam and Block (1978), Sinha et al. (1981), Gharib and Rosko (1987) and Howe (1997) among others).

From the theoretical viewpoint, vortex sheet type models had been introduced by Stuart (1967) and further used to study flow with detached shear-layer (Ziada and Rockwell (1982), Ho and Huerre (1984), and Howe (1996)) leading to successful predictions of the vortex-leading-edge interactions, of the momentum thickness growth and of the Strouhal number values.

The importance of the growth of vorticity perturbations in the shear layer has been pointed out time ago. Although it has been shown to transform into a vortex-like structure and to play a fundamental role for the overall dynamic inside and outside the cavity, there only exist little information concerning the dynamical characteristics of these vortices.

The present experimental work is therefore dedicated to the characterization of vortices standing at the ‘mouth’ of the cavity. Flow at a very low Mach number is favored to simplify and allow high accuracy of the measurement based on a ‘non intrusive’ optical technique. This choice restricts the present work to a rather fundamental study of cavity flows out of the scope of usual “real life” aero-acoustic applications. Despite this limitation, it is believed that accurate experimental vortex characteristics at very low Mach number are still essential to compare with results from Direct Numerical Simulation.

Our experimental approach is primarily based on particle image velocimetry (PIV). This technique allows to obtain detailed instantaneous 2D velocity component fields of the airflow. The laser sheet is produced by a Nd-YAG laser delivering double pulses at a repetitive rate of about 5 Hz. The range of velocity of the flow and the low repetition rate of the image recording does not allow chronological recordings (as it would be the case in water flow (Lin and Rockwell 2001)). Therefore, vortices cannot be tracked against time since the time lapse between two double pulses of PIV measurements is about ten times larger than the residence time of a vortex.

The velocity fields derived from the PIV images are further post-processed through the vorticity variable. At this level, the selectivity of a wavelet operator is used to localize in space a vortical pattern similar to a Lamb-Oseen’s type vortex. The database of velocity fields is reduced to an ensemble of vortices characterized by some quantities such as core location, core size, core velocity, rotation sign, and energy content. These results are then displayed in a local averaged presentation.

## 2. EXPERIMENTAL APPARATUS

### 2.1. Wind tunnel description

The experimental investigations were conducted in an open circuit, subsonic wind tunnel installed vertically. The channel is operated by a centrifugal type blower ensuring a low speed velocity in the range of 1 to 20 m/s. The cross section dimensions of the test section of this wind tunnel are 300x100 mm<sup>2</sup>. A schematic view of this test section is depicted in Figure 2.

The entire measurement campaign was made on a rectangular cavity with a constant step height ( $h = 20$  mm.) and a constant cavity length ( $L = 80$  mm). Therefore the expansion ratio (the ratio of the total height of the test section to the height of the upstream test section) is equal to 1.2 and the aspect ratio (ratio of the spanwise test section length to the step height of the cavity) is equal to 15.

### 2.2 Inlet conditions

Preliminary hot wire measurements have been made to characterize the incoming flow conditions. This investigation of the boundary layer was reported as a critical issue to characterize the cavity flow (Karamcheti (1955), Sarohia (1977)). Three streamwise locations upstream of the separation edge (i.e.  $x/h=0$ ,  $x/h=1$ ,  $x/h=3$ ) were investigated for two different free stream velocities (associated with  $Re_h = 4000$  &  $9000$ ). During these measurements, the data were sampled at 3 kHz during 10 seconds at different  $y/h$  stations. These experimental points compare well with a Blasius’s laminar profile (Schlichting (1968)). In Table 1 parameters such as Reynolds number, boundary layer thickness, displacement thickness and momentum thickness shown in dimensionless form are presented to characterize the type of incoming boundary layer. Since the shape factor,  $H$  (the ratio between displacement thickness and momentum thickness), would be about 1.3 for a turbulent boundary layer and 2.6 for a

laminar boundary layer over a flat plate (Schlichting (1968)), this table also shows that the incoming boundary layer is clearly a laminar one (if we accept inaccuracy on the computation of  $H$  based on integration of measured velocity profiles).

	$Re_h$	$\delta/h$	$\delta^*/h$	$\theta/h$	$\delta^*/\delta$	$H$
CASE 1	4000	$28.7 \times 10^{-2}$	$9.3 \times 10^{-2}$	$3.5 \times 10^{-2}$	0.32	2.66
CASE 2	9000	$22.8 \times 10^{-2}$	$6.9 \times 10^{-2}$	$2.8 \times 10^{-2}$	0.30	2.46
CASE 3	13000	$20.7 \times 10^{-2}$	$6.2 \times 10^{-2}$	$2.5 \times 10^{-2}$	0.30	2.48

**Table 1: Dynamical parameters of the incoming boundary layer**

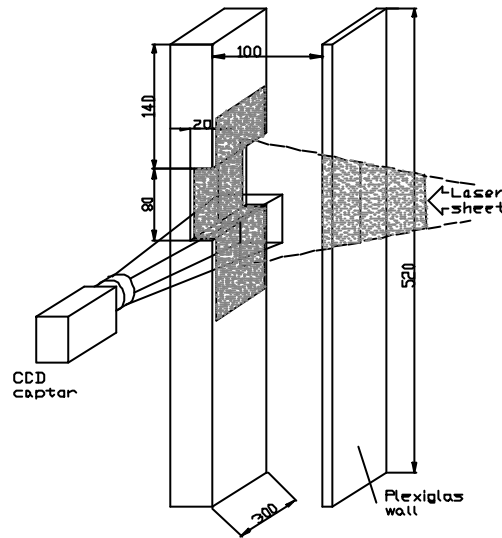


Figure 2: Test section of the cavity flow with sketch of the camera and of the laser sheet

### **2.3 Technical aspect of PIV measurements**

It is not the goal of this article to present a state of the art of PIV, nevertheless interested readers are invited to consult Raffel et al. (1998) or Scarano (2002) for a review.

In the present study, the laser sheet was generated by a 200 mJ Nd:YAG double-pulsed laser. Cylindrical lenses were arranged to produce a laser sheet of 0.5 mm thickness. A smoke generator was used to seed the flow with fine oil droplets ( $\sim 1 \mu\text{m}$ ). A digital CCD cooled camera (PCO Sensicam with a resolution of  $1280 \times 1024$  square pixels) recorded the successive images at 4.9 Hz with a region of interest limited to  $1280 \times 832$  pixels. The pulse separation between two images of the same PIV couple was corresponding to a maximum displacement over the whole field of about 8 pixels (with  $\Delta T = 40 \sim 130 \mu\text{s}$ ). The spatial calibration gave a length of  $52 \mu\text{m}$  corresponding to 1 pixel on the image.

The PIV measurements are performed in a field of view of  $67 \times 43 \text{ mm}^2$ . In order to keep a high resolution over the region of interest, the entire measurement domain was split in two areas with an overlapping border. The first area (called hereafter upstream) was capturing the leading edge of the cavity; the second one (called hereafter downstream) was capturing the trailing edge of the cavity. These two regions were combined to investigate the whole cavity. It has to be underlined that the spatial resolution in both parts of the cavity was kept equal and that the time tracking of individual vortices was not the scope of our study (velocity fields are uncorrelated in time).

The PIV acquisition parameters are collected in Table 2.

Acquisition parameters	case1 ( $Re_h=4000$ )	case2 ( $Re_h=9000$ )	case3 ( $Re_h=13000$ )
image size	[1280x832] px <sup>2</sup>	[1280x832] px <sup>2</sup>	[1280x832] px <sup>2</sup>
calibration	$\sim 5.2 \times 10^{-2}$ mm/px	$\sim 5.2 \times 10^{-2}$ mm/px	$\sim 5.2 \times 10^{-2}$ mm/px
pulse separation	130 $\mu$ s	56 $\mu$ s	37 $\mu$ s
frequency of acquisition	4.9 Hz	4.9 Hz	4.9 Hz
number of samples	1000 couples/zone	1000 couples/zone	1000 couples/zone

Table 2: PIV acquisition parameters

### 3. PROCESSING LEVELS OF THE RAW DATA

#### 3.1. PIV processing: From the particle images to the velocity vector fields

In each area of interest (upstream and downstream), a number of one thousand image couples have been acquired and pre-processed with the homemade cross-correlation algorithm: WIDIM (WIndow Displacement Iterative Multigrid). This program is based on an iterative multigrid predictor-corrector method, handling the window distortion (to better resolve the shear flows) and the sub-pixel window displacement (to limit the pixel-locking) (Scarano and Riethmuller 2000). In this multigrid approach, the prediction-correction method was validated for each grid size if the Signal to Noise Ratio of the correlation was above a threshold of 1.5 (Scarano and Riethmuller, 1999). This ratio is defined as the value of the displacement peak divided by the second maximum. In average, less than 1% of the vectors are detected as spurious vectors (case where  $SNR < 1.5$ ) and are flagged to be re-interpolated using a bilinear scheme. The final and finest grid used by this algorithm was composed of 24 by 24 pixel<sup>2</sup> size interrogation window and overlapped by 50% leading to a vector spacing of 12 by 12 pixels<sup>2</sup>.

After this processing a total of 1000 instantaneous velocity fields were obtained for each case.

Accuracy of the measurements is a major concern, especially when the derivatives of the velocity are of interest. The systematic error, which appears mainly as the so-called pixel-locking phenomenon, was assessed by displaying histograms of particle displacement. The histogram shows a bimodal distribution that is associated to the mean stream displacement for the highest peak value and to the inside cavity displacement for the lower peak. Indeed, the tracer's image diameter ( $D_p \cong 3$  pixels by a visual check) was sufficient to limit this inherent effect (Westerweel, 1998).

The parameters of the PIV processing are given in Table 3.

sub-pixel fitting scheme	Gaussian
Window Distortion	1 <sup>st</sup> order
Final window size	[24x24] px <sup>2</sup>
Overlap	[12x12] px <sup>2</sup> (50 %)
Final number of vectors	[105x68]
Number of bad vectors / Total vectors	less than 1 %

Table 3: WIDIM processing parameters

From this ensemble of instantaneous velocity vector fields, classical ensemble averages were computed and will be presented in the next section (i.e. maps of scaled mean velocity with streamlines, maps of scaled velocity component standard deviation and maps of scaled Reynolds stress).

#### 3.2. Post-processing: From the instantaneous quantities to the vortex based statistics

##### 3.2.1. Wavelet coefficient fields

A recognition algorithm is used to extract vorticity pattern when a set of user-defined conditions is satisfied.

A brief but self-contained description of this algorithm is given hereafter (for completeness refer to Schram et al. (2003)).

From each velocity vector field, the vorticity is estimated with a central and symmetrical four points stencil (3<sup>rd</sup> order Richardson finite difference scheme). This vorticity field is then squared to increase the “signal to noise ratio” and further analyzed with a continuous wavelet approach.

Basically, a wavelet operator has the property to be compactly defined both in the spatial domain and in the frequency domain (Farge (1992)). A generic wavelet shape is called a mother wavelet. A wavelet family composed of one hundred members is created from the mother wavelet through dilatation or contraction. Each family member is associated to the size of the support upon which the wavelet function is not vanishing. For vortex pattern detection, a Maar’s wavelet family is used (i.e. Mexican Hat wavelet). The choice of this mother wavelet has proved to be well adapted to vortex detection (Farge (1992), Schram et al. (2003)).

Each wavelet member is used as a local filter on the square vorticity field and the result is one wavelet coefficient field associated to this scale. All wavelet coefficient fields are gathered in a 3D matrix inside of which a search for local maxima wavelet coefficients is performed. At a given spatial location, a vortex is tagged as a possible vortex if the corresponding wavelet coefficient is a local maximum over the scales.

### 3.2.2. Local rotation field

Before accepting a pattern of vorticity as a vortex in the database, a test on the local rotation of the flow is performed. Following Jeong and Hussain (1995), the flow is locally mainly rotating if  $\lambda_2$  is negative ( $\lambda_2$  is the second eigenvalue of the tensor  $S_{ik}S_{kj} + \Omega_{ik}\Omega_{kj}$  with  $S$  and  $\Omega$  respectively the symmetrical and anti-symmetrical part of the tensor gradient of velocity). The two-dimensional version of this criterion is used here to filter out the pure shear area occupied by the shear-layer. In the present application, the threshold related to  $\lambda_2$  has been fixed to four times the standard deviation computed by only taking into account negative values of  $\lambda_2$ . This empirical value has been visually found to be high enough to filter out the shear layer-like events but not too high to still capture the vortex-like events (see example section 3.3).

### 3.2.3. Scaling and comparison with calibration

A Lamb-Oseen’s vortex is used to derive a relation between vortex core diameter and scale of the better-fitted wavelet member. The core of Lamb-Oseen’s vortex is defined as the diameter of the region for which the tangential velocity is linearly increasing (Schram et al. (2003)).

Each wavelet coefficient of a vortex candidate is compared to the wavelet coefficient given by Lamb-Oseen’s vortex of the same core. This comparison leads to a successful validation if the “resemblance” with a Lamb-Oseen’s vortex is superior to 50%. This primitive test was originally designed to reduce confusion between a single vortex and two pairing ones covering the same area.

### 3.2.4. Acceptance to enter in the vortex data base

A candidate vortex is accepted if three conditions are met. It has to be a local maximum over the wavelet coefficients (3.2.1). It has to correspond with a location of strong rotation (3.2.2). It has to be in a close resemblance with the calibrating vortex of this scale (3.2.3).

If these three conditions are met the following information are incorporated on the database: spatial location of the vortex center, core size, velocity of the vortex center, vorticity sign and circulation value around the core.

### 3.3. A practical example of vortex detection

In this paragraph, identification is shown through a step-by-step example.

On Figure 3 (a), an instantaneous velocity vector field obtained after the PIV processing is presented (upstream configuration). This field of view includes several vorticity patches as shown on Figure 3 (b). At this point, it is important to remind that although a vortex presents always a peak of vorticity, a peak of vorticity is not always a vortex. In particular, the presence of a detached shear layer is clearly noticeable. Figure 3 (c) shows that  $\lambda_2$  criterion will clearly filter out the non-purely rotating part of this vorticity field. Finally, Figure 3 (d) presents the location of three vortex candidates extracted by the wavelet algorithm from the flow field displayed in Figure 3 (a). This simple example shows that the presented algorithm making use of a given set of threshold values is capable of correctly extract the vortices from a given flow field.

## 4. RESULTS AND DISCUSSIONS

The following results will be presented into two main categories. The first one is concerned with classical ensemble average of the mean velocity modulus, velocity components standard deviation and Reynolds stress results.

The second part focuses on the new information given by the vortex database.

In both parts, the results are non-dimensionalized.

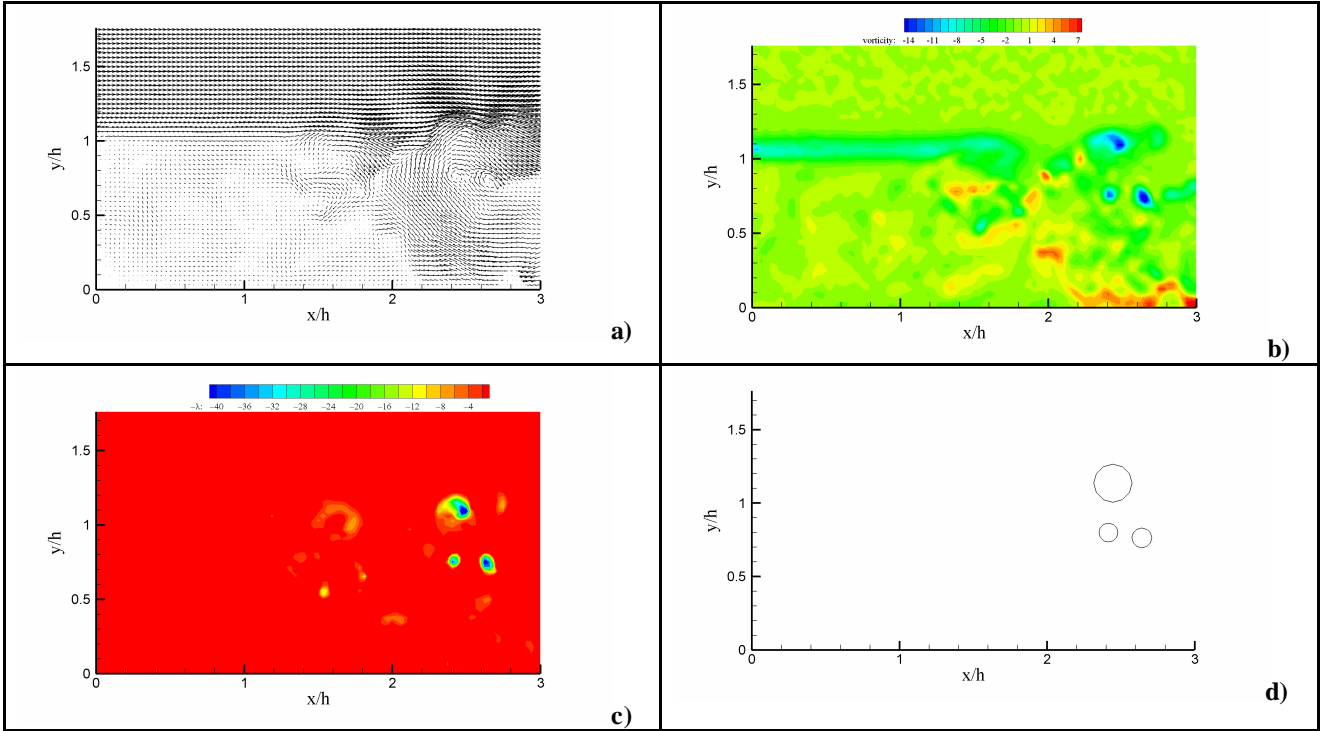


Figure 3: a- Instantaneous vectors flow field. b- Instantaneous vorticity field. c- Instantaneous negative lambda field. d- Result of the vortex detection

#### 4.1. Results based on ensemble averaging and Reynolds decomposition of the PIV fields

The distribution of the velocity modulus and the associated streamlines inside and outside the cavity for the three Reynolds number are presented in Figure 4 (a). In all the cases, the streamlines pattern depicts two main recirculation bubbles filling the whole cavity. The first bubble (upstream) is rotating counter-clockwise whereas the second bubble (downstream) is rotating clockwise. Following the cavity designations reviewed by Komerath et al. (1987), the present measurements are taken in a shallow cavity ( $L/h > 1$ ) and the cavity was found to be of an open type (there is no streamline connecting directly the leading edge or the trailing edge to the bottom of the cavity). Furthermore, it is observed that the centers of the first and second recirculation bubbles are moving in the upstream direction when the Reynolds number increases. In a square lid-driven cavity Ghia et al. 1982 (in Shankar and Deshpande 2000) found the same movement of the primary vortex when the Reynolds number passed from 100 to 10000. It may be roughly estimated that this clockwise recirculation bubble occupies 60% ( $Re_h = 4000$ ), 72% ( $Re_h = 9000$ ) and 82% ( $Re_h = 13000$ ) of the whole cavity surface and the de-attachment point on the bottom of the cavity separating the two bubbles is located in the interval  $[2.5h; 3.0h]$  ( $Re_h = 4000$ ),  $[2.0h; 2.5h]$  ( $Re_h = 9000$ ) and  $[1.5h; 2.0h]$  ( $Re_h = 13000$ ).

Figure 4 (b) presents the streamwise velocity component standard deviation. The highest value of this quantity (non-dimensionalized by the free stream velocity) is about 0.2 in the three cases. It is noticeable that the area surrounded by the contour associated with the value 0.18 increases with the Reynolds number.

On the contrary, the same area associated with the other velocity component standard deviation decreases when the Reynolds number increases (Figure 4 (c)). This phenomenon, already observed by Karamcheti (1955) and Komerath et al. (1987), is due to the Kelvin-Helmholtz instabilities that are giving to the shear layer stronger periodical oscillations when the flow outside the cavity is laminar at low Reynolds number. With a higher Reynolds number (toward turbulent flow outside the cavity) these shear-layer oscillations had been observed to be less significant (Karamcheti (1955)).

In Figure 4 (d), the Reynolds stress is shown in a dimensionless form taking as a reference value the free stream velocity to the square. It is found that the Reynolds number has a weak influence on the maximum value of this variable. Nevertheless, it is observed that the location of the maximum shear stress is moving towards the leading edge when the Reynolds number increases (as it was the case for the center of the cavity recirculation bubbles). In Figure 5, Reynolds stress values are plotted along a line situated at  $y/h = 1$ . On the left, semi-log scale representation versus distance from the leading edge scaled by the momentum thickness is proposed. It is found that this figure follows the results of Gharib and Roshko (1987). In this reference, the authors were using an axi-symmetrical cavity operated with water under three different Reynolds number values (based on the free stream velocity and the momentum thickness).

They found out that the maximum Reynolds stress was exponentially growing till a region of saturation. It was then decreasing before the trailing edge. In the present work similar behavior is found with a slight difference.

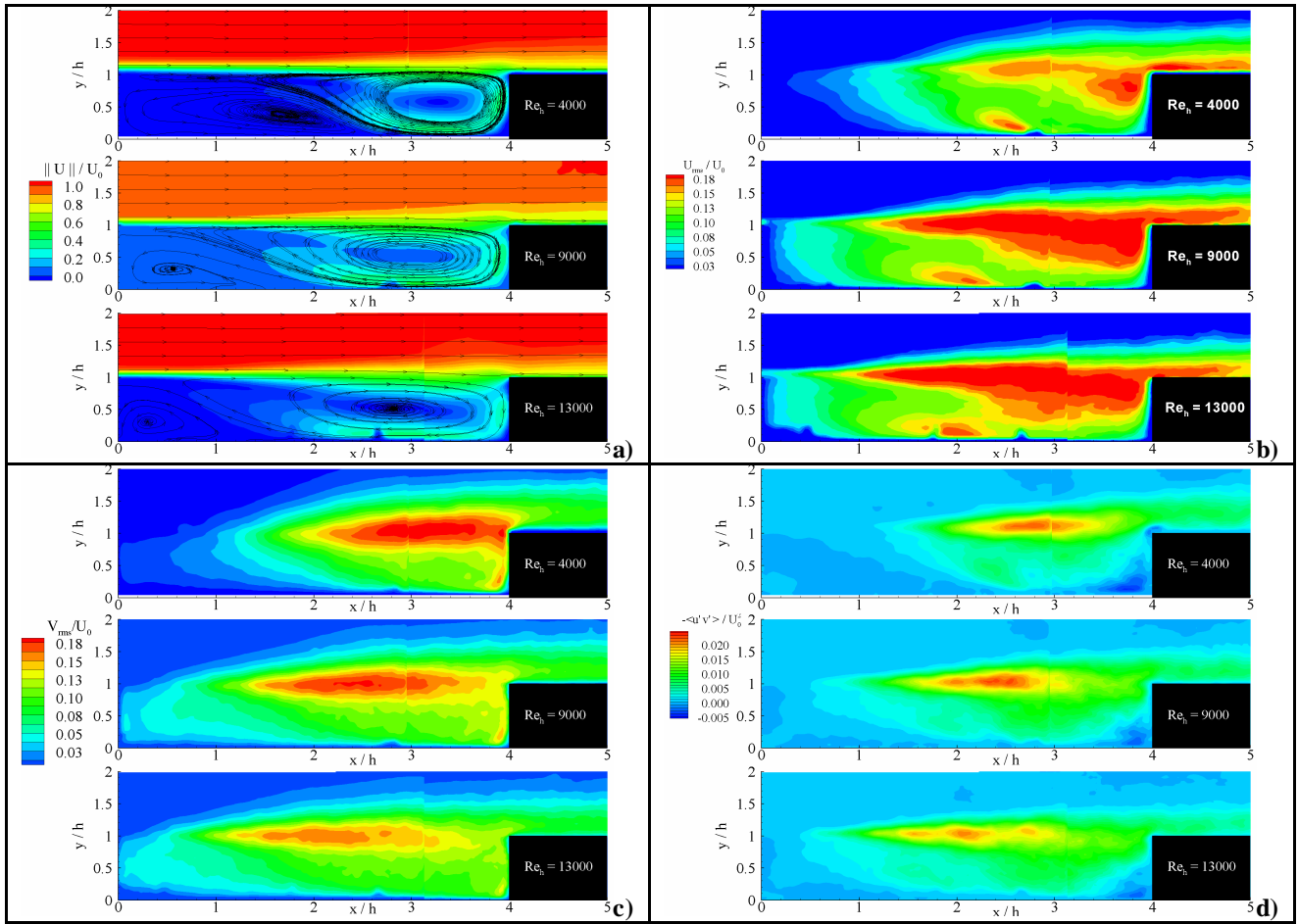


Figure 4: a- Map of velocity modulus and streamlines for an increasing Reynolds number. b- Map of  $u_{rms}$  for an increasing Reynolds number. c- Map of  $v_{rms}$  for an increasing Reynolds number d- Map of Reynolds stress for an increasing Reynolds number.

In their experiments Gharib and Roshko (1987) were working in the range of  $Re_\theta \in [85; 130]$  in comparison of  $Re_\theta \in [160; 366]$  in the present work. In Figure 5 (a), the squared symbols represent the variation of the maximum shear stress along the cavity entry for  $Re_\theta = 160$ . This growth is following an exponential law (the slope is almost linear in semi-log), in a case associated with the highest oscillation of the shear layer. For the two other Reynolds numbers ( $Re_\theta = 260$  &  $366$ ), the growth is closer to a linear law characterizing a weaker oscillation of the shear layer (the slope is not following a line in semi-log). It is a confirmation that the shear layer exhibits larger oscillations when the free stream flow is more laminar (i.e. Karamcheti (1955)). On the axial cavity of Sarohia (1977) at  $Re_\theta = 242$ , the growth of the shear layer was found almost linear but no information was given on the associated growth of the shear stress. The Reynolds number ( $Re_\theta$ ) of this last reference is in the range of  $Re_\theta$  for which a linear growth of the maximum Reynolds shear stress is presumed in our results. Figure 5 (b) displays the same Reynolds shear stress in a linear representation and with a distance scaled by the cavity depth. The rather slow growth associated to  $Re_\theta = 160$  until  $X/h = 1$  and then the exponential growth after this abscissa has to be compared with the earlier growth of  $Re_\theta = 260$  &  $366$ . On this graph, differences on the saturation values for the Reynolds shear stress are noticeable. The discontinuity associated with  $Re_\theta = 160$  at  $X/h = 3$  is due to the passage from the upstream to the downstream measurement fields. This jump may be interpreted as a different degree of convergence between the two measurement fields (upstream, downstream) at this low Reynolds number associated with the higher flapping magnitude of the shear layer.

## 4.2. Results based on eduction of vortices with wavelet filtering

### 4.2.1. Results based on the full database

In Figure 1, an overview of the vortices extracted for the three measurement campaigns is proposed. This figure presents all the positions and relative sizes of the vortices extracted and collected in the vortex database. For clarity, the vortex cores are not displayed in their real size spanning from 0.12h to 0.54h. Nevertheless, it is noticeable that the size of the larger vortices embedded in the shear layer is decreasing with the Reynolds number. It is thought that this fact is linked with the size of the momentum thickness of the incoming boundary layer that is also decreasing when the Reynolds number increases.

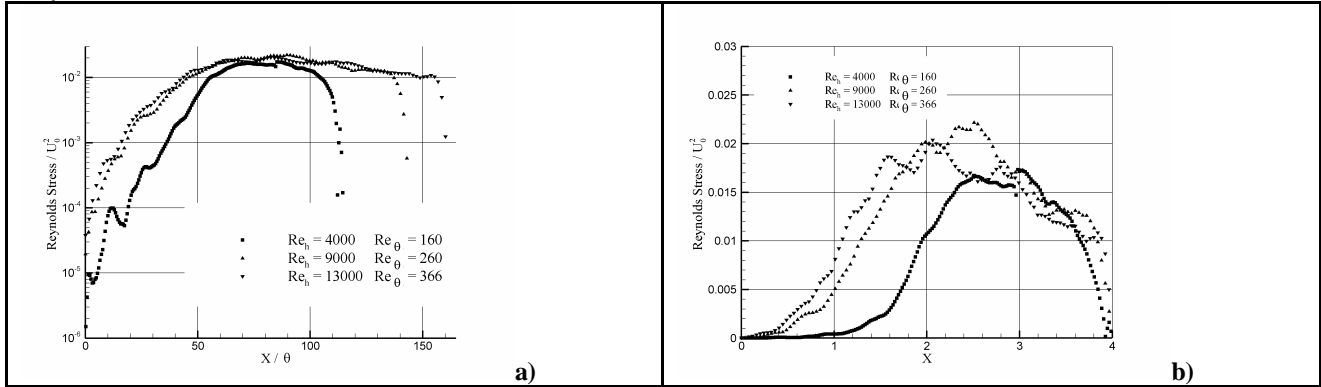


Figure 5: Growth of the maximum shear stress (at  $y/h = 1$ .) in the cavity shear layer versus downstream distance (a - Semi-log Scaled by momentum thickness, b - Scaled by cavity depth)

In Figure 1 one can also notice that, for the three cases, the pattern drawn by the presence of the vortices gives the idea of a “jet” attached to the leading edge. Indeed, previous works have attempted to describe the shear driven cavity with the help of a virtual jet coming from the trailing edge (i.e. edge tones theory (Howe 1997)) where the shear layer is modeled as a vortex sheet. In this last reference the author gives what he called a *naïve* picture as:

”Wall aperture and cavity operating stages are associated with a feedback mechanism involving the periodic formation of discrete vortices near the leading (upstream) edge (Rossiter 1962). Each vortex is convected over the opening during a time of order  $L/U_c$ , at a velocity  $U_c$  that is typically about half the free-stream speed  $U$ . An impulsive disturbance is generated when the vortex reaches the downstream edge which initiates the formation of a new vortex.”

Indeed, the present authors find this picture interesting even if such a mechanism cannot be observed with our statistical approach (except for the convection velocity of vortices as it is displayed in the next paragraph).

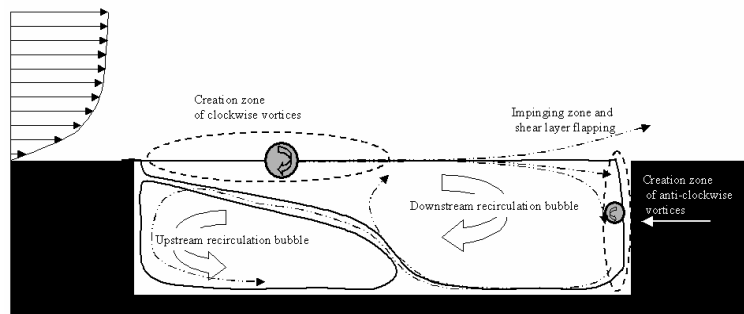


Figure 6: Schematic drawing of the cavity flow

Figure 6 proposes a simplified illustration of the flow observed by the present authors. On this figure, recirculation bubbles are drawn together with location, path and sign of vortices. This simple drawing is only a guideline to analyze Figure 1. It shows that vortices present within the shear layer and inside the cavity may be classified according to their rotation signs, i.e. clockwise and counter-clockwise. It appears that the clockwise vortices seem to be created in the shear layer close to the leading edge. These vortices are then convected in the downstream direction with the possibility to enter in the cavity, to pass over it or to impinge on the trailing edge. The vortices entering inside the cavity are mainly located in the clockwise recirculation bubble. In the lower Reynolds number case associated with the higher fluctuations of the shear layer and the larger vortices imbedded inside the same shear layer, it is found that a more important amount of counter-clockwise vortices is present. These last vortices are created along the trailing wall (higher concentration of counter-clockwise vortices in the down right corner of the cavity in the Figure 1 for  $Re_h = 4000$ ). The mechanisms controlling the formation of this category of induced vortices have been well capture by the visualization

of Tang and Rockwell (1983) as a consequence due to the path of a primary vortices (from the leading edge shear layer) over the cavity or impinging on the trailing edge. These second type of vortices seem to be driven by the clockwise recirculation bubble towards the region inside of the cavity separating the two bubbles. Afterwards, these vortices seem to be trapped mainly in the counter-clockwise recirculation bubble or released out of the cavity.

When the Reynolds number increases, the occurrence of large clockwise vortices decreases as well as the standard deviation of the velocity component driving the flow inside and outside the “mouth” of the cavity. As a consequence the presence of counter-clockwise vortices inside of the cavity and along the trailing wall is strongly reduced.

Figure 7 (a, b & c) are displaying the core size of extracted vortex versus their dimensionless circulation (the core diameter is divided by initial momentum thickness). On these three figures, the ratio vortex core / initial momentum thickness is increasing faster with the absolute values of the circulation when the  $Re_h$  increases. For the smallest Reynolds number, a broader distribution of dimensionless circulation is found. This quantity is found by summation of the vorticity on a surface limited by the core diameter. It can be observed that these distributions are not symmetrical with respect to the vertical axis. This lack of symmetry is thought to be due to the vorticity magnitude and the momentum thickness of the two different shear layers (the one attached to the leading edge and the wall shear along the trailing wall). It is clear that vortices with core size smaller than the initial momentum thickness were probably present in the cavity but were not taken into account (because of the limited resolution). In Figure 7 (c), it appears that only a small number of counter-clockwise vortices are extracted in comparison with the two other cases. We can see in these figures the limitations of the algorithm used for the vortex extraction and especially the circulation estimation: a few data belonging to the negative vorticity populations are lying in the positive circulation field. This illustrates the limits of accuracy of the technique.

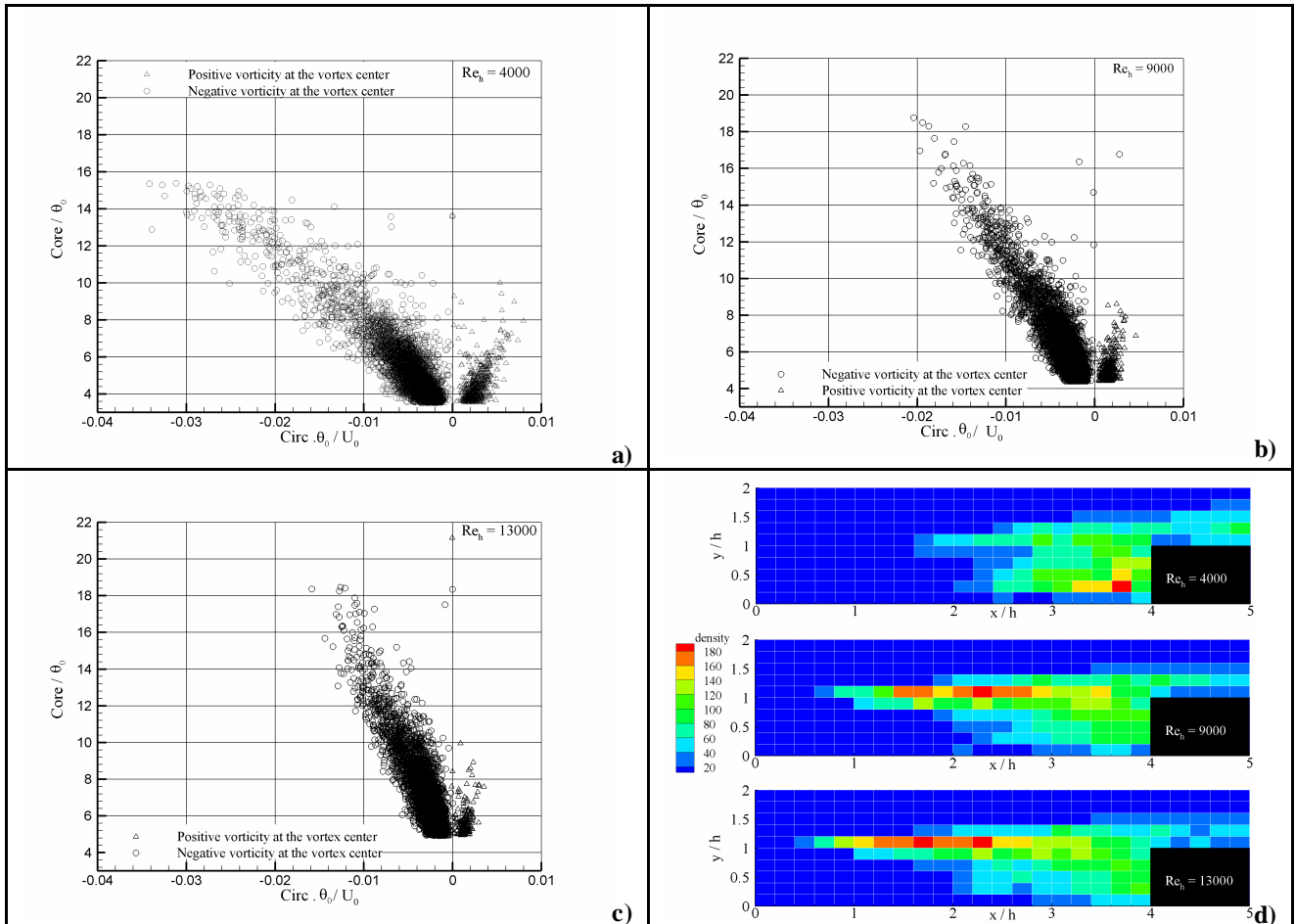


Figure 7: a - Dimensionless core size versus dimensionless circulation for the cavity at  $Re_h=4000$  ( $q_0$  is the initial momentum thickness). b - Dimensionless core size versus dimensionless circulation for the cavity at  $Re_h=9000$  ( $q_0$  is the initial momentum thickness). c - Dimensionless core size versus dimensionless circulation for the cavity at  $Re_h=13000$  ( $q_0$  is the initial momentum thickness). d - Density number of vortices detected.

#### 4.2.2. Results based on local spatial averaging of the database

In the previous paragraph of this paper, distributions of vortices were presented without local averaging. In the present one, local average velocity modulus of vortices is presented. These local average are obtained in two steps.

First, the ensemble of detected vortices (Figure 1) is projected on a Cartesian regular mesh.

The cell size is chosen such that a sufficient number of vortices by cell is obtained, yielding a statistically meaningful local average of their characteristics but that it is small enough to allow a good resolution. After several trials, the cell size is taken as  $0.2h \times 0.2h$ . For each cell, the number density of vortices is determined (i.e. number of vortices by cell). The density field thus obtained is shown in Figure 7 (d). It is noticeable that the high-density areas are moving in the upwind direction when the Reynolds increases. This shift is also found in the classical average presented in Figure 4 (a, b, c & d).

Visually the zones of higher vortex density are very similar to zones of higher standard deviations of the two velocity components even if a perfect matching is not expected due to the relatively low amount of vortices in the vortex-database. The area associated with the Reynolds shear stress saturation corresponds to the higher density of extracted vortices (Figure 8). One can judge that the tendencies are very similar in this arbitrary scaled comparison even if it is still necessary to find a proper scaling factor to establish this link numerically.

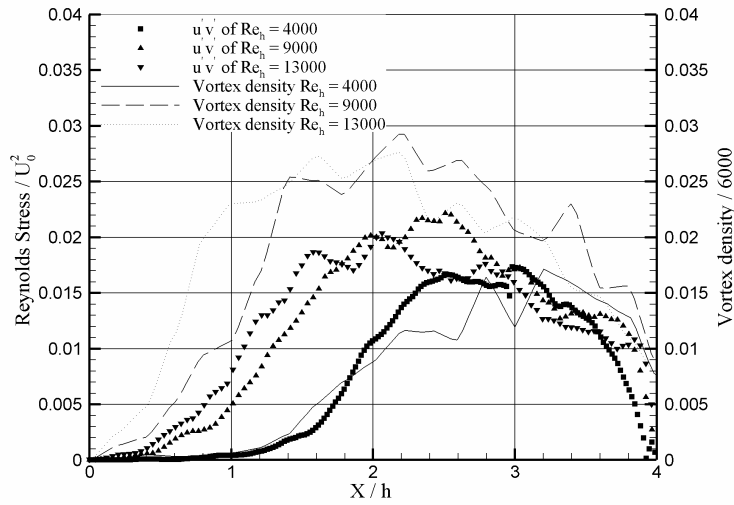


Figure 8: Comparison of shear stress values at the mouth of the cavity and associated density of extracted vortices

The local ensemble average velocity of the vortex structures in each cell ( $\tilde{U}$ ) is also calculated. The velocity of one extracted vortex was defined as the flow velocity measured at the location of the maximum of vorticity. A picture of this local ensemble average velocity divided by the free stream velocity is shown in Figure 9. In this figure, whenever the number of the vortices in a cell was found to be less than 100, the window was blanked (i.e. not taken into account) to avoid possible errors introduced by statistically meaningless data. The non-dimensional value of the averaged velocity of the vortices is found to vary between 0.4 to 0.5. This value is in close agreement with Howe (1997) who proposed a value of the scaled convection vortex speed of the order of 0.5. These measured values are also in agreement with the linear stability results of Ziada and Rockwell (1982, Vol. 124) associated to velocity of instability inside of a shear layer impinging upon an edge. At higher Mach number Larcheveque et al. (2003) are using two different techniques to extract the convection velocity from their Large Eddy Simulation. The first one is using two-point/two-time velocity correlations from which they found a convection velocity ranging from 0.4 to 0.7 at the mouth of the cavity. In a second part of their works they classify vortices into three categories respectively flying over the cavity, impinging the trailing edge corner or entering inside of the cavity. The convection speed is deduced from the time derivative of the vortex location. At this level they were able to propose three convection velocity curves associated with each vortex category. It is observed that vortices entering inside the cavity are the slower with a scaled convection velocity of about 0.2 to 0.4. The two other vortex categories are associated with convection speed of 0.4 to 0.7. Such time resolved results were not considered in our uncorrelated measurements so that a cruder approximation of the vortex velocity is proposed. Nevertheless knowing that no distinction is done on the class of vortices found on the line  $y/h = 1$ , the present results certainly deserve to be extended to a wider database.

Indeed more accurate vortex characteristics over a larger part of the cavity should be obtained by increasing the number of vortices therefore by increasing the number of particle image velocimetry fields. It has been found that this local

conditional statistic is more costly in term of images to be taken than a classical statistic (for standard accuracy and level of confidence).

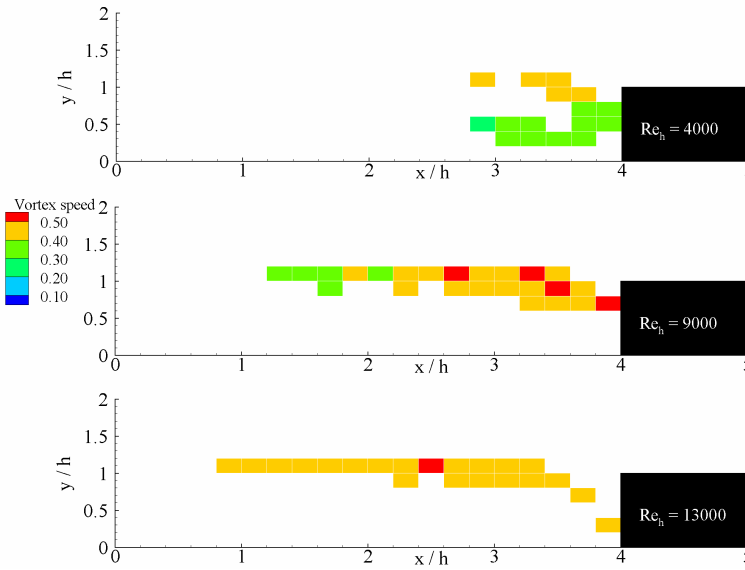


Figure 9: Local average of scaled vortices velocity modulus (displayed when density number is over 100)

## 5. CONCLUSIONS

In the present work an extensive amount of Particle Image Velocimetry data has been taken to study a shallow cavity flow under three different Reynolds numbers. The aim of the wavelet-based post-processing is to automate the extraction of the vortex contents from the measurements. If these vortices play a fundamental role in the dynamics of the flow inside and outside the cavity, a statistical description of their characteristics was missing. In order to propose a first set of characteristics, a cavity with length to depth ratio ( $L/h = 4$ ) under an incoming laminar boundary layer was selected. The sensitivity to the Reynolds number has been analyzed.

In all cases, cavity flows were belonging to an open type and were mainly characterized by two large circulation bubbles turning in opposite directions. As the Reynolds number increased, the downstream recirculation bubble became larger and its center moved towards the leading edge. Consequently, the upstream recirculation decreased in size. The enlargement of the downstream recirculation bubble with increasing free stream velocity is attributed to the increasing energizing effect of the shear layer.

An increase of the Reynolds number led to an increase of the area of higher scaled streamwise velocity standard deviation (with a maximum value of about 20%). On the contrary, an opposite tendency is observed for the scaled standard deviation associated with the V component as it has been previously reported in the literature.

On the map of dimensionless Reynolds shear stress, the Reynolds number has been found to have a weaker influence on the maximum value level and on the associated area. Nevertheless, it is noticeable that the location of the maximum Reynolds shear stress is moving towards the leading edge. This position of the saturated value is linked to the growth of Reynolds shear stress on the mouth of the cavity. With the lower Reynolds number, this growth is slow at first and becomes then exponential in comparison to the two other cases where the growth is happening sooner following a linear slope.

The novelty of the present work consists in the vortex-based statistics. An overview of the position occupied by the vortices was found similar to a jet attached to the leading edge. Two main areas of vortex production were identified. Clockwise vortices were created inside of the shear layer when counter-clockwise vortices were mainly created by the trailing wall-layer. The concentration of these vortices at lower Reynolds number seems to be higher in the trailing edge recirculation bubble and in an area in between the two-recirculation bubbles.

The size of the vortices is presented scaled by the initial momentum thickness of the incoming boundary layer.

A qualitatively good comparison is found between shear stress curves and concentration of extracted vortices at the mouth of the cavity.

A local average of number of vortices is proposed and it confirms that the concentration of the vortices at higher Reynolds number behaves as a jet-like pattern. The velocity of the vortices is found to be of the order (but less) than half of the free stream velocity. It is believed that a larger number of realizations would improve the precision associated to this estimation.

It is believed that 10000 vector fields would have been necessary to provide an accuracy of these vortex statistics comparable to classical statistics such as mean velocity of the air flow. Further measurements together with sensitivity analysis are currently planned to improve the confidence.

## REFERENCES

- Farge M. (1992) "Wavelet transforms and their applications to turbulence". *Ann. Rev. Fluid Mech.* 24: 395-457.
- Gharib M. and Roshko A. (1987) "The effect of flow oscillations on cavity drag", *J. Fluid Mech.*, Vol. 177, pp. 501-530.
- Ho C.M and Huerre P. (1984) "Perturbed free shear layers" *Ann. Rev. Fluid Mech.* 16:365-424.
- Howe M.S. (1997) "Edge, cavity and aperture tones at very low mach numbers", *J. Fluid Mech.* Vol. 330, pp. 61-84.
- Jeong J. and Hussain F. (1995) "On the identification of a vortex", *J. Fluid Mech.* Vol. 285, pp. 69-94.
- Karamcheti K. (1955) "Sound Radiation from rectangular cutouts" NACA TN 3488.
- Komerath N.M., Ahuja K.K., Chambers F.W. (1987) "Prediction and measurement of flows over cavities. A survey." AIAA 25<sup>th</sup> Aerospace Sciences Meeting, January 12-15 Reno, Nevada.
- Larchevêque L., Sagaut P., Mary I., Labbé O., Comte P. (2003) "Large-eddy simulation of a compressible flow past a deep cavity" *Physics of Fluids*, Vol. 15, No. 1, pp. 193-210.
- Lin J.C., Rockwell D. (2001) "Organized oscillations of initially turbulent flow past a cavity" *AIAA Journal*, Vol. 39, No. 6, June 2001.
- Raffel M.; Willert C.; Kompenhans J. (1998) "Particle Image Velocimetry – Practical Guide" (Ed. Springer, Berlin)
- Rockwell D., Naudascher E. (1978) "Review – Self-sustaining oscillation of flow past cavities" *Journal of Fluids Engineering*, Vol. 100, June 1978.
- Sarohia V. (1977) "Experimental investigation of oscillations in flows over shallow cavities" *AIAA Journal* Vol. 15, No. 7.
- Scarano F. (2002) "Iterative image deformation methods in PIV". *Meas. Sci. Technol.* 13: R1-R19.
- Scarano F. and Riethmuller M.L. (1999) "Iterative multigrid approach in PIV image processing with discrete window offset" *Experiments in Fluids* Vol. 26, pp. 513-523.
- Scarano F.; Riethmuller M.L. (2000) "Advances in iterative multigrid PIV image processing." *Exp Fluids* 29: S51-S60.
- Schlichting H.(1968) "Boundary Layer theory", Six Edition, Mc Graw-Hill Book Company. pp:129.
- Schram C.; Rambaud P.; M.L. Riethmuller (2004) "Wavelet based eddy structure eduction from a backward facing step flow investigated using particle image velocimetry." *Experiments in Fluids* 36, 233-245. DOI 10.1007/so 0348-003-0695-9
- Shankar P. N. and Deshpande M. D. (2000) "Fluid mechanics in the driven cavity" *Annu. Rev. Fluid Mech.* 32: 93-136.
- Sinha S.N., Gupta A.K., Oberai M.M. (1982) "Laminar separating flow over backsteps and cavities. Part II: Cavities" *AIAA Journal*, Vol. 20, No. 3, March.
- Stuart J.T. (1967) "On finite amplitude oscillation in laminar mixing layers" *J. Fluid Mech.*, Vol. 29, Part 3, pp.417-440.
- Tam C.K.W., P.J.W. Block (1978) "On the tones and pressure oscillations induced by flow over rectangular cavities", *J. Fluid Mech.*, Vol. 89, Part 2, pp. 373-399.
- Tang Y.P., Rockwell D. (1983) "Instantaneous pressure fields at a corner associated with vortex impingement" *J. Fluid Mech.*, Vol. 126, pp. 187-204.
- Westerweel J. (1998), "Effect of sensor geometry on the performances of PIV interrogation", 9<sup>th</sup> symposium on Applications of Laser Techniques to Fluid Mechanics, July 1998, Lisbon
- Ziada S., Rockwell D. (1982) "Vortex-leading-edge interaction" *J. Fluid. Mech.* Vol. 118, pp.79-107.
- Ziada S., Rockwell D. (1982) "Oscillations of an unstable mixing layer impinging upon an edge" *J. Fluid Mech.* Vol. 124, pp. 307-334.